Contributed paper

OPTO-ELECTRONICS REVIEW 7(1), 1–17 (1999)

$Al_xGa_yIn_{1-x-y}As$/InP-based quantum well infrared photodetectors

C. JELEN and M. RAZEGHI*

Center for Quantum Devices, Department of Electrical and Computer Engineering, Northwestern University, Evanston, IL 60208, USA

In order to tune the wavelength of a lattice-matched quantum well infrared photodetector (QWIP) over the range 3–20 μm, new designs are demonstrated for the first time which utilise $Al_xGa_yIn_{1-x-y}As$ layers lattice-matched to InP and grown by gas-source molecular beam epitaxy. We demonstrate 8, 13, and 18– μm QWIPs using the lattice-matched n–doped $(Al_xGa_{1-x})_{0.48}In_{0.52}As$ /InP system. We also review QWIP structures of $Ga_{0.47}In_{0.53}As/Al_{0.48}In_{0.52}As$ grown on InP substrate with peak photoresponse at 4 μm. Combining these two materials, we report the first multicolour detectors that combine lattice-matched quantum wells of $Ga_{0.47}In_{0.53}As/Al_{0.48}In_{0.52}As$ and $Ga_{0.47}In_{0.53}As$/InP. Utilising two contacts, a voltage tunable, lattice-matched, two colour QWIP with a peak wavelength of 8 μm at a bias of V = 5 V and a peak wavelength of 4 μm at V = 10 V is demonstrated. Using the measured noise data for $Ga_{0.47}In_{0.53}As$/InP detectors, we have calculated the thermal generation rate, bias-dependent gain, electron trapping probability, and electron diffusion length. The calculated thermal generation rate (~ 7×10^{22} $cm^{-3}s^{-1}$) is similar to $Al_xGa_{1-x}As$/GaAs QWIPs with similar peak wavelengths, but the gain is 50 times larger, indicating improved transport and carrier lifetime are obtained in the binary InP barriers.

Keywords: AlGaInAs/InP QWIPs, infrared photodetectors, multicolour detectors

1. Introduction

The proliferation of powerful, inexpensive computers and new sensor technologies that are responsive to the infrared (IR) regions of the electro-magnetic spectrum has made possible many new detector applications. Research groups working in image processing are showing increased interest in fusing the information from various sensor combinations, such as IR and visible, or multiple-IR bands. Military applications driving the demand for sensor fusion include automatic target detection, definition, and recognition as well as night vision and surveillance imagery. Alongside this is the rapid growth in the civil and commercial fields of applications of this technology which stretch from crime prevention to crop disease detection.

One of the major problems encountered when attempting to assemble a multi-band sensor is that single-band images must be registered to achieve a good fused image. Even if the sensors have matching fields-of-view, complete pixel registration cannot be achieved. Differences in rotation, lens magnification, chromatic aberration, and distortion can all lead to pixel misregistration. Generally, two non-registered images must be registered using computer-processing techniques to stretch the images and interpolate the pixel values; a computationally intensive operation that cannot easily be achieved in real-time.

The more elegant approach to multi-band imaging is to perform the sensor fusion at the focal plane level. This eliminates the need for pixel registration, provided that an appropriate multi-band detector array can be monolithically integrated on a single substrate. Two-colour infrared detectors designed for dual band applications often require integrated mid-wavelength infrared (MWIR) and long-wavelength infrared (LWIR) focal plane arrays. This objective has been difficult to achieve due to the lattice mismatch between commonly used interband MWIR and LWIR

*e-mail: razeghi@ece.nwu.edu

infrared materials such as InSb and HgCdTe. For this reason, stacks of lattice-matched multi-quantum well intersubband photodetectors have been proposed for use in multicolour infrared detectors.

The quantum well infrared photodetector (QWIP) is based on intersubband absorption by confined carriers in multiple quantum wells. QWIPs have a narrow absorption spectrum that can be tailored to match any transition in the 3–20 µm wavelength range by adjusting the quantum well width and barrier layer composition. More important, it can be made using mature III-V semiconductors based on gallium arsenide (GaAs) or indium phosphide (InP).

Since infrared absorption due to intersubband transitions was first observed in multiple quantum well (MQW) structures [1], quantum well infrared photodetectors and arrays based on this principle have become a competitive infrared technology [2]. Because of the extensive scientific and commercial exploration of the AlGaAs/GaAs material system over the past decades, the application of this technology to 8–12-µm long-wavelength infrared (LWIR) MQW detectors has rapidly reached commercial maturity.

Recently, other material systems have been investigated. For some applications, MQW detectors lattice-matched to InP substrates have several advantages in comparison to LWIR MQW detectors composed of $GaAs/Al_xGa_{1-x}As$:

1. The effective mass of electrons, which governs the drift mobility and tunneling properties, amounts to $0.042m_o$ in $Ga_{0.47}In_{0.53}As$ compared to $0.067m_o$ GaAs, where m_o is the free-electron mass;
2. Mid-wavelength infrared (MWIR) 3–5 µm $Ga_{0.47}In_{0.53}As/Al_{0.48}In_{0.52}As$ quantum well detectors are lattice-matched with LWIR $Ga_{0.47}In_{0.53}As/InP$ QWIP detectors, allowing a 2-colour MWIR-LWIR lattice-matched detector stack to be grown on InP. This minimum intersubband absorption wavelength that can be achieved in $GaAs/Al_xGa_{1-x}As$ QWIPs is 6 µm [3].

Since the photoresponse spectrum of an $Ga_{0.47}In_{0.53}As/InP$ QWIP has a maximum at approximately 8 µm [4], the use of $Ga_xIn_{1-x}As_yP_{1-y}$ quantum wells has been studied [5] to allow longer wavelength ($\lambda \sim 12$ µm) detection. Because the AlGaInAs material system covers approximately the same bandgap energies as GaInAsP, it is interesting to compare the hot electron transport and performance of quantum well infrared photodetectors fabricated from these two materials. In this paper, we demonstrate that high quality quantum well infrared photodetectors in the 3–5 µm, 8–12 µm, and 12–20 µm spectral bands can all be grown on InP substrate using gas-source molecular beam epitaxy of $Al_xGa_yIn_{1-x-y}As$ materials.

2. Quantum well infrared photodetector design and operation

2.1. Background

Suggestions to use optical transitions between quantum confined subband states for infrared (IR) applications were made in the early days of quantum well research [6,7]. The study of intersubband optical transitions in doped MQWs was motivated by possibilities of fabricating high-speed sensitive IR photodetectors and fast modulators. The first observations of intersubband transitions were made by West and Eglash [1] in GaAs–AlGaAs multiple quantum wells (MQWs). The first unambiguous demonstration of a quantum well infrared photodetector (QWIP) was also made in GaAs–AlGaAs by Levine et al. at AT&T (now Lucent) Bell Laboratories [8]. Since that publication, other groups have studied intersubband optical transitions in quantum wells of GaAs/AlGaAs (for a review see Ref. 9), GaInAs/AlInAs [10], GaInAs/InP [4,11–14], GaAs/GaInP [15–19], and SiGe/Si [20]. Both conduction band (n–type) and valence band (p–type) quantum wells have been studied, although the large effective mass results in poorer responsivity for the p–type devices. For that reason, this review will focus on n–type devices only.

2.2. Overview of intersubband detector operation

The cross section of a typical QWIP device is shown in Fig. 1. The operation of an n–type QWIP is easily summarised using the bandgap profile shown in Fig. 2. Upon application of an electric field, incident photons excite electrons out of the quantum wells, creating a photocurrent. The wells are doped to provide a population of carriers in the ground state subband. The device operation of QWIPs is similar to that of conventional semiconductor photoconductors. The distinct feature of QWIPs is that incident photons are only absorbed in discrete quantum wells, which are much narrower in width than the inactive confinement barrier regions. Other quantitative differences between QWIPs and conventional intrinsic or extrinsic photodetectors are that QWIPs possess high oper-

 © 1999 COSiW SEP, Warsaw

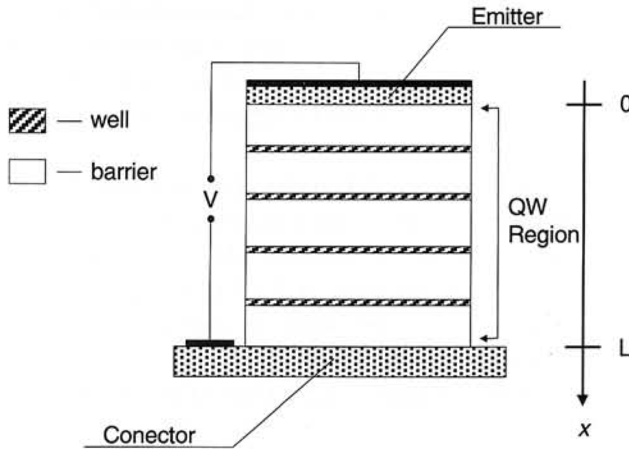

Fig. 1. Cross-section of a typical QWIP structure.

ating electric fields, long carrier mean free paths in comparison to the device thickness, and high device speeds. Furthermore, unlike most conventional photoconductors, QWIPs have highly nonlinear current-voltage characteristics.

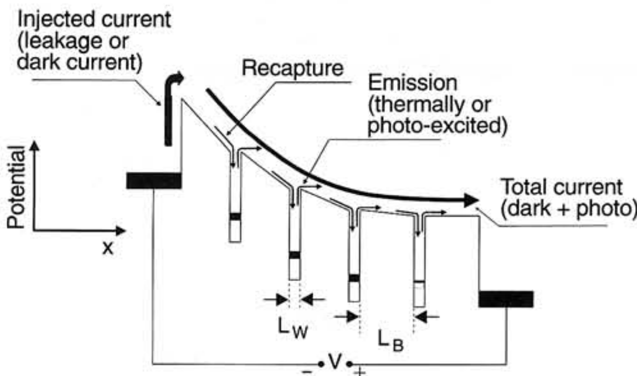

Fig. 2. A conduction band potential diagram for an n–type QWIP illustrating the sources of dark and photocurrents.

The peak internal quantum efficiency η_{int} of a bound-to-bound QWIP for unpolarised light is given by [21]

$$\eta_{\mathrm{int}} = \frac{1}{2}\left[1-\exp\left(-3.258\times10^{-3}\,\frac{N_d W f_Q\, sN}{\Gamma}\sin^2\theta\right)\right] \tag{1}$$

where s is the number of times a photon passes through the detector, N is the number of periods in the MQW structure, N_d is the doping density in 10^{18} cm^{-3}, W is the well width in Å, Γ is the absorption line width broadening factor in meV, θ is the angle of the light with respect to the normal to the quantum well, and f_Q is the oscillator strength, ≅ 1.

When a light beam propagates normal to the quantum well layers, θ = 0°, and there is no appreciable intersubband absorption. Unfortunately, most detector applications rely on this incident geometry. Therefore, in actual detector applications where normal incident geometry has been adopted, the incident light must be redirected inside the sample (i.e. θ > 0) based on certain coupling schemes in order to achieve absorption.

Once the quantum efficiency is known, the number of carriers generated by incoming photons is given by

$$\dot{N} = \eta Q A_d \text{ (carriers/second)} \tag{2}$$

where Q is the photon flux density and A_d is the detector area in units of cm^2.

However, not all of the generated carriers will actually arrive at the contacts and contribute to the photocurrent signal. The total number of photoexcited carriers "alive" at any time is the produce of their generation rate times their mean lifetime. Thus, the carrier concentration n is the total number of carriers alive divided by the volume of the sample

$$n = \frac{\dot{N}\tau}{A_d L} \tag{3}$$

The photodetector current is the product of the carrier concentration n, the mean drift velocity v_d, the charge e on the electron, and the detector area A_d

$$\mathrm{I} = nev_d A_d \tag{4}$$

The mean drift velocity is defined as the mobility μ times the electric field E. E is calculated as the voltage V across the detector divided by the inter-electrode spacing L

$$v_d = \mu E \tag{5}$$

Combining equations (2)–(5) together gives the photocurrent

$$I = \eta Q A_d e \frac{\mu\tau E}{L} = \eta Q A_d e g \tag{6}$$

The quantity μτE/L is dimensionless and is named the photoconductive gain. Depending on the design of the QWIP detector and operating bias, it can be as large as several hundred or as small as one-hundredth.

2.3. Optical coupling requirements for QWIPs

QWIPs do not absorb radiation incident normal to a wafer surface since the light polarisation does not have an electric field component normal to the growth direction, as it is required for absorption by the confined carriers, see Eq. (1). As a consequence, single QWIP detectors are usually illuminated through a 45° polished facet [22], Fig. 3(a). Two-dimensional arrays based on etched facets have been demonstrated by Chen et al. [23]. Efficient light coupling can also be achieved by reflecting the IR radiation off of monolithically integrated gratings, Fig. 3(b). This technique, developed by Sarusi et al. [24,25], and Andersson et al. [26,27], is utilised in current commercially available QWIP IR imaging sensors.

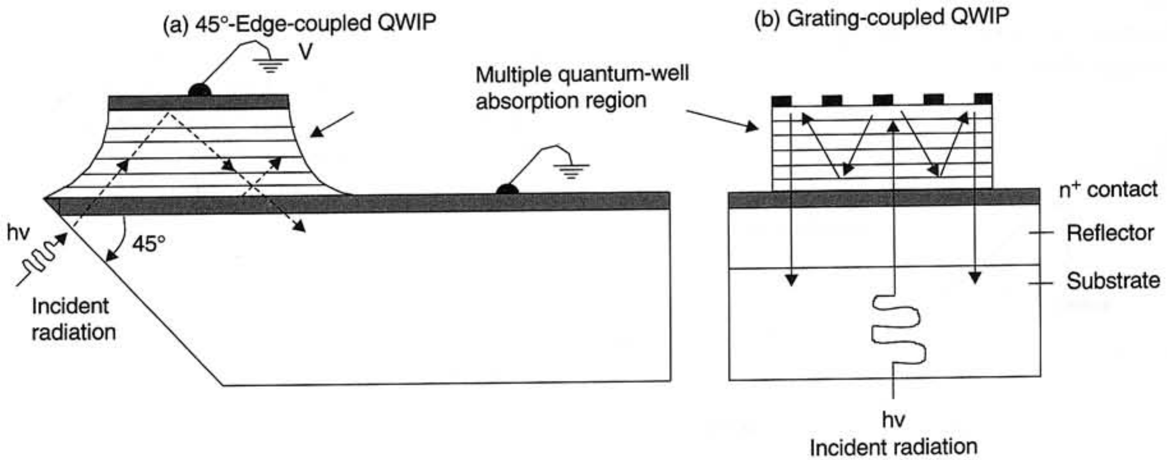

Fig. 3. Different light-coupling mechanisms used in QWIPs: (a) 45° polished facet, (b) two-dimensional gratings (after Ref. 9).

3. Growth and characterisation of AlGaInAs/InP-based materials

Although two quaternary III-V systems are available for InP-based opto and microelectronics: $Ga_xIn_{1-x}As_yP_{1-y}$ and $Al_xGa_yIn_{1-x-y}As$, only the former has been extensively studied. However, the $Al_xGa_yIn_{1-x-y}As$ system is seen as a possible replacement for $Ga_xIn_{1-x}As_yP_{1-y}$ alloys in some lasers and photodetectors because the concentration of only two (Al and Ga) of its constituents need to be adjusted to vary the bandgap while retaining lattice matching, whereas in the $Ga_xIn_{1-x}As_yP_{1-y}$ system the ratio of all four of its constituents must be altered. A number of investigators have demonstrated the growth of $Al_xGa_yIn_{1-x-y}As$ alloys on InP substrates for a variety of electronic device applications [28–30], but no QWIPs using $Al_xGa_yIn_{1-x-y}As/InP$ quantum wells have previously been reported. Since the devices presented in this section are the first ever demonstrated, a comparison is instead made with the $Ga_xIn_{1-x}As_yP_{1-y}/InP$ QWIPs reported by Gunapala, et al. [5].

The growth of the AlGaInAs alloy is relatively easier than GaInAsP due to the following reasons [31]:

1) only one group V element (As) is incorporated, avoiding the problem of As/P ratio control;
2) composition of the layer is controlled by each constituent element flux intensity [32],
3) near-unity sticking coefficients of the three group III elements facilitate reproducibility of composition.

The bandgap of AlGaInAs alloy can be engineered between the emission wavelengths of the two boundary ternary alloys, namely; $Ga_{0.47}In_{0.53}As$

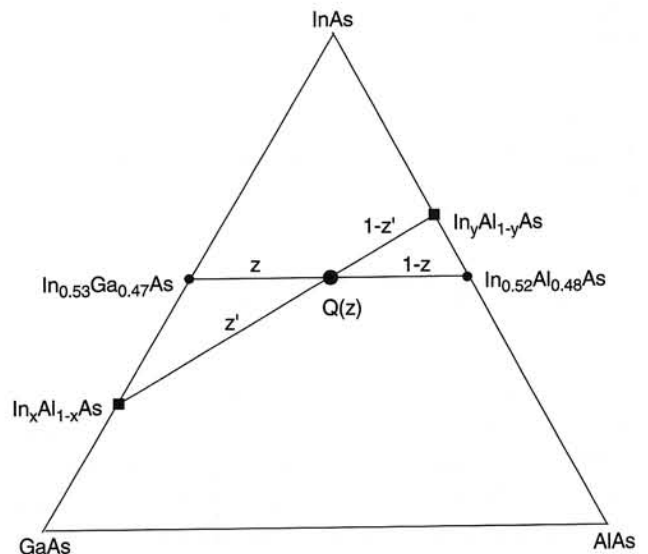

Fig. 4. Any InP lattice-matched AlGaInAs quaternary Q(z) can be obtained by superimposing either lattice-matched or mismatched ternaries.

 © 1999 COSiW SEP, Warsaw

Table 1. Growth conditions used for GSMBE growth of AlGaInAs

Material	RHEED pattern	Growth temperature (K)	Temperature relative to (2 × 1) to (2 × 4) transition	Group V flux (sccm)	Growth rate (Å/min)
AlGaInAs	(2 × 4)	500	$T_T + 30$	5	220

(0.76 eV, 1.63 μm) and $Al_{0.48}In_{0.52}As$ (1.46 eV, 0.85 μm). Thus any alloy composition can be considered a pseudo-binary superposition of $Ga_xIn_{1-x}As$ and $Al_yIn_{1-y}As$, as shown in Fig. 4. The bandgap of $(Al_xGa_{1-x})_{0.48}In_{0.52}As$ lattice-matched to InP is shown in Figure 5 as a function of aluminum composition x.

The $(Al_xGa_{1-x})_{0.48}In_{0.52}As$ growth conditions used for the QWIP detectors reported here are given in Table 1.

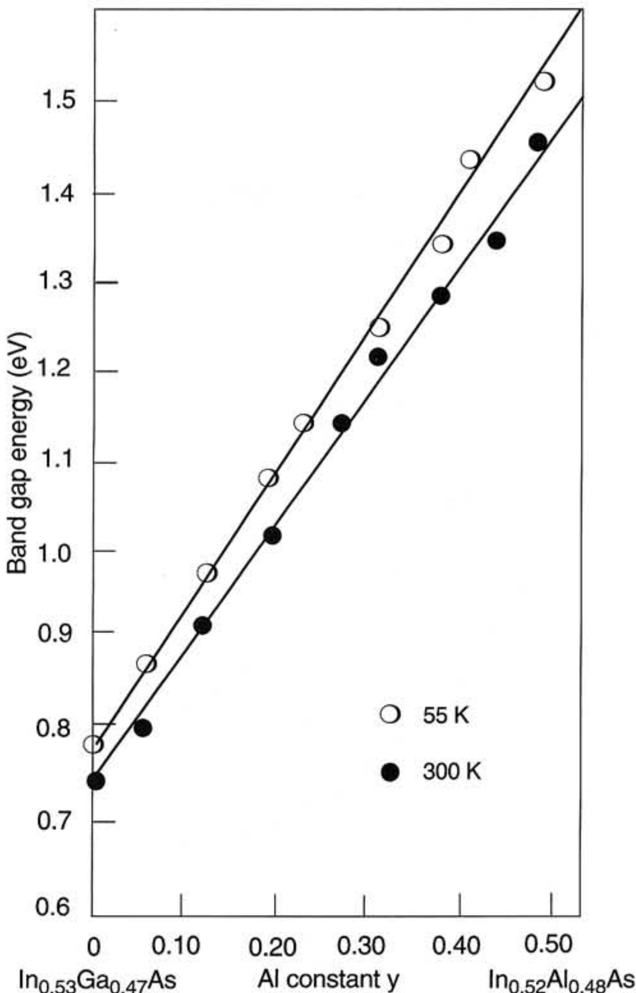

Fig. 5. Bandgap energy of AlGaInAs alloys lattice-matched to InP as a function of Al mole fraction.

4. Characterisation and analysis of AlGaInAs/InP and GaInAs/AlInAs QWIP detectors

4.1. Device design

The device parameters of the QWIPs studied are listed in Table 2, where L_B represents the barrier width, L_W is the well width, and N_D denotes the donor doping concentration of the quantum wells. The wafers were grown using an EPI modular Gen–II gas-source molecular beam epitaxy system equipped with arsine and phosphine sources for As and P. Metallic gallium and indium were used for group III elements. The devices were grown on semi-insulating InP (100) substrates. After epitaxial growth, standard photolithographic process is used to fabricate mesa photodetectors.

A square active area of 1.6×10^{-3} cm^2 was defined and 1600 Å–thick AuGe/Ni/Au ohmic contacts were deposited by electron beam evaporation and patterned using a lift-off process.

4.2. Detector characterisation

4.2.1. Long-wavelength InGaAs/InP QWIPs

The spectral response of QWIP-A at 80 K was measured using a Mattson Fourier transform IR

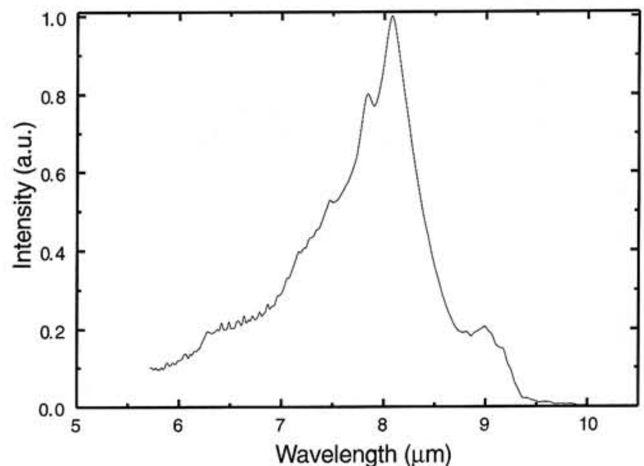

Fig. 6. Normalised spectral response at T = 80 K and V = 10 kV/cm bias demonstrates a peak at 8.1 μm for QWIP-A.

Table 2. Device parameters for the measured QWIPs

QWIP	Barrier material	L_W (Å)	Well material	L_B (Å)	N_D (cm^{-3})	Periods
A	InP	56	$In_{0.53}Ga_{0.47}As$	500	5×10^{17}	20
B	InP	60	$In_{0.53}Ga_{0.47}As$	500	5×10^{17}	20
C	$Al_{0.48}In_{0.52}As$	30	$In_{0.53}Ga_{0.47}As$	400	2×10^{18}	25
D	$Al_{0.48}In_{0.52}As$	35	$In_{0.53}Ga_{0.47}As$	400	2×10^{18}	25
E	$Al_{0.48}In_{0.52}As$	40	$In_{0.53}Ga_{0.47}As$	400	2×10^{18}	25
F	InP	60	$In_{0.52}Ga_{0.38}Al_{0.1}As$	500	5×10^{17}	25
G	InP	65	$In_{0.52}Ga_{0.33}Al_{0.15}As$	500	5×10^{17}	25

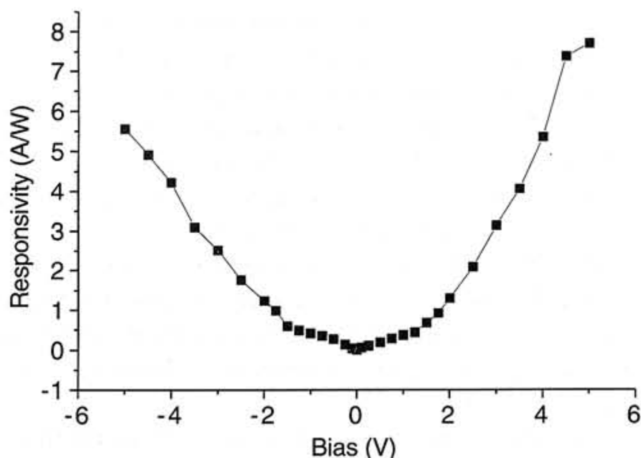

Fig. 7. Responsivity for InGaAs/InP QWIP-A at T = 77 K as a function of bias.

spectrometer (GL3020). Absolute responsivity was measured using a Mikron blackbody source (M305) chopped at 500 Hz and an EG&G 5209 lock-in amplifier. The blackbody temperature was 800 K. Peak responsivity was calculated by integrating the normalised spectral response with the blackbody responsivity. The normalised spectrum under an applied electric field of 10 kV/cm is shown in Fig. 6.

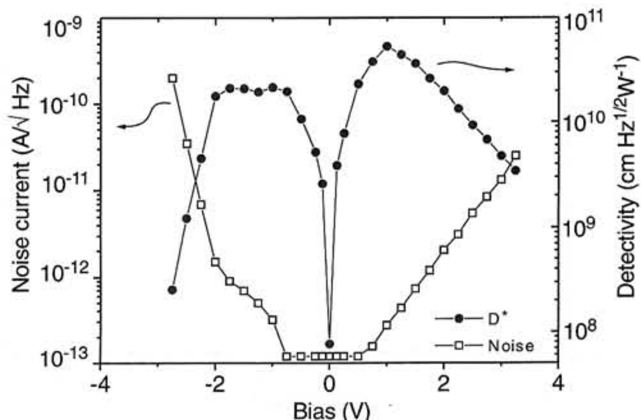

Fig. 8. Noise and detectivity for InGaAs/InP QWIP-A at T = 77 K as a function of bias.

The photoresponse peak is found to be 8.1 μm and the 50% cutoff wavelength is 8.5 μm. The absolute responsivity is shown in Fig. 7 as a function of bias.

The peak responsivity value of 7.5 A/W at 5 V reverse bias is approximately one order of magnitude higher than that typically obtained in GaAs/AlGaAs QWIPs. The specific detectivity (D*) and noise current of the QWIP at 80 K are shown as a function of applied electric field in Fig. 8. The maximum D* of the QWIPs measured in this work was found to be 5×10^{11} cmHz$^{1/2}$W^{-1} at 1.2 V.

4.2.2. Mid-wavelength infrared GaInAs/AlInAs QWIPs

In order to determine the wavelength range at which GaInAs/AlInAs QWIPs can operate, we have calculated the energy levels in GaInAs/AlInAs MQW structures. For this calculation, we have assumed $m_{well} = 0.041m_o$, $m_{barrier} = 0.075m_o$, $E_{g77Kwell} = 1.508$ eV,

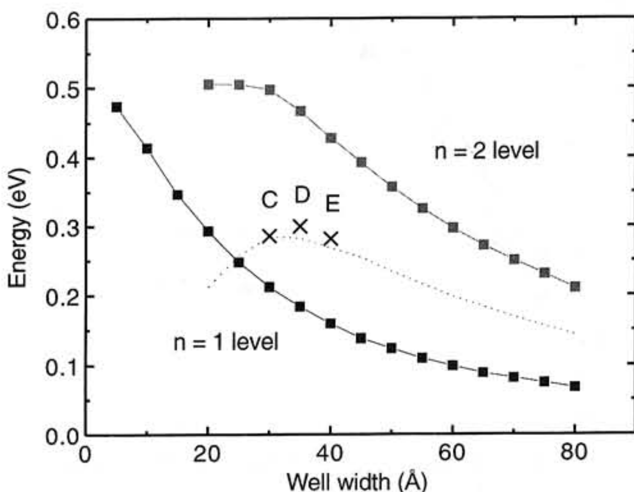

Fig. 9. The calculated two first electron levels in GaInAs/AlInAs quantum wells (solid lines) vs well width. Experimental data points obtained for samples C–E are shown as well.

 © 1999 COSiW SEP, Warsaw

$E_{g77Kbarrier}$ = 0.801 eV, and ΔE_c = 0.5 meV. In Fig. 9 the n = 1 and n = 2 electron energy levels are plotted versus the well width. The n = 2 level is confined to the well for well widths larger than 35 Å, and is an extended state for narrower wells. For wells thicker than 35 Å the intersubband absorption energy is calculated from the energy difference between the n = 1 and n = 2 states. For narrower wells the absorption energy is calculated from the difference in energy between the confined n = 1 and the center of the continuum band. The experimental data points for samples C–E are also shown, demonstrating good agreement with our model calculations.

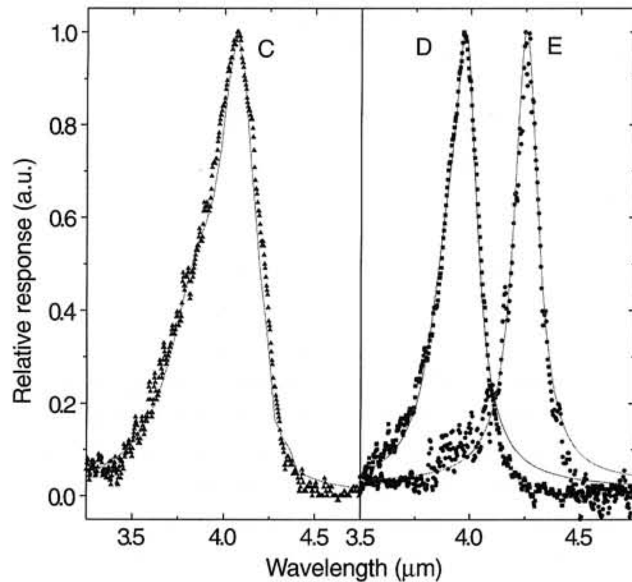

Fig. 10. Measured spectral responsivity of samples C–E at T = 77 K with 1 V reverse bias.

The result of the measurement is shown in Fig. 10. All three samples have significantly narrower spectrum than reported for strained $Ga_{0.8}In_{0.2}As/Al_{0.38}Ga_{0.62}As$ QWIPs [33]. The difference in spectral width when the well is changed from L_w = 30 Å to 40 Å is in excellent agreement with our theoretical calculations. According to the calculations, the first excited state for the 30 Å sample is in the continuum, resulting in a broad absorption spectrum. On the other hand, the excited state in the 35 Å sample is just slightly bound (quasi-bound), and in the 40 Å sample is more strongly bound. In either case, the intersubband absorption for both is narrow in excellent agreement with experiment. To our knowledge, the spectral width ($\Delta\lambda$ = 0.13 μm) of sample E is the narrowest reported for a QWIP.

4.2.3. Very long-wavelength AlGaInAs/InP QWIPs

For these experiments, three structures were grown. The AlAs mole fraction of the $Al_xGa_{0.48-x}In_{0.52}As$ material and the quantum well width for the three samples were (x = 0, 56 Å), (x = 0.1, 60 Å), and (x = 0.15, 65 Å) respectively, as listed in Table 2.

The responsivity spectrum of the three samples measured at T = 10 K are shown in Fig. 11. For a bias of –1 V (mesa top negative), the 50% long wavelength cutoff wavelengths for the three samples were 8.5, 13.3, and 19.4 μm, respectively. The peak and cutoff wavelengths, and linewidth $\Delta\lambda/\lambda$ for the three samples are given in Table 3.

Table 3. Spectral response parameters for the three samples studied

Sample	Peak wavelength (μm)	Cutoff wavelength (μm)	FWHM ($\Delta\lambda/\lambda$)
A	8.1	8.5	12.5%
F	12.7	13.3	8%
G	19	19.5	9%

The bias dependence of the responsivity was measured for samples A and F at T = 77 K and the results are shown in Fig. 12 for both positive and negative bias. The responsivity of sample G was too low to be measured at T = 77 K. The peak responsivity at –1 V of the $Al_{0.1}Ga_{0.38}In_{0.52}As/InP$ QWIP (sample F) was 0.37 A/W. This is comparable (20% higher) to the GaInAsP/InP QWIP (1.3 μm bandgap, L_W = 63 Å) reported by Gunapala et al. [5] which had a similar

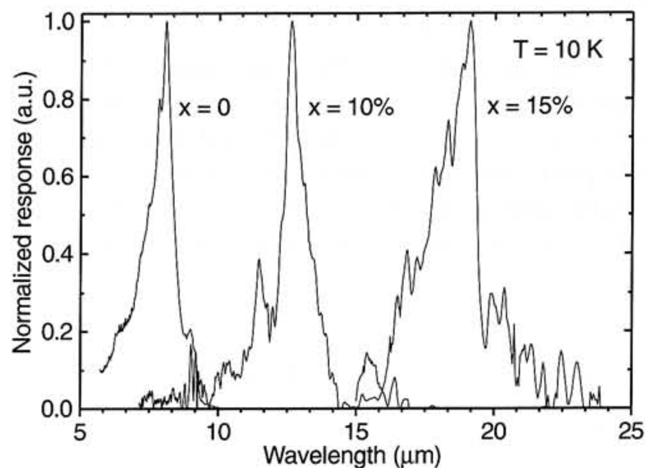

Fig. 11. Normalised spectral response for $Al_xGa_{0.48-x}In_{0.52}As/InP$ QWIPs with x = 0, x = 0.1, and x = 0.15 mole fraction of AlAs.

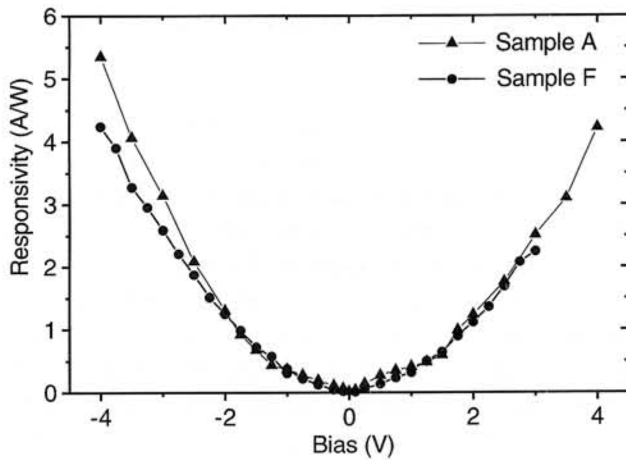

Fig. 12. Bias dependence of peak responsivity measured at T = 77 K for InGaAs/InP (sample A) and $Al_{0.1}Ga_{0.38}In_{0.52}As$/InP (sample F) QWIPs.

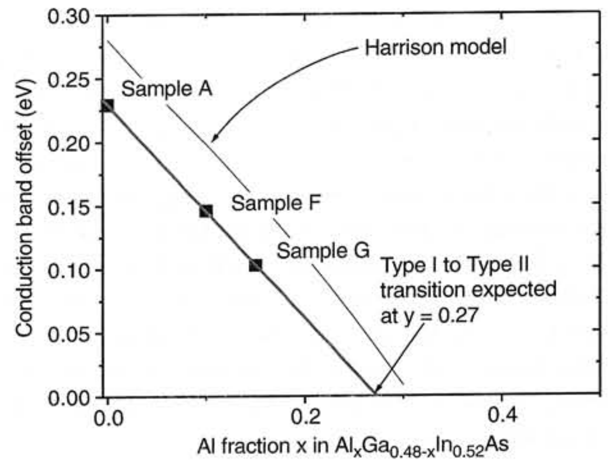

Fig. 13. Conduction band offset values calculated from samples A, F, and G as a function of Al fraction y in $Al_xGa_{0.48-x}In_{0.52}As$. Also shown is a theoretically derived curve by Ishikawa et al. [36].

13.2 μm cutoff wavelength. It is worth noting the responsivity for these samples is approximately five times as large as the best responsivity measured for GaAs/AlGaAs QWIPs.

The noise current, i_n, of the $Al_{0.1}Ga_{0.38}In_{0.52}As$/InP and $Ga_{0.47}In_{0.53}As$/InP QWIPs was measured at T = 77 K as a function of bias voltage using a spectrum analyzer and found to be i_n = 80- and 0.4-pA, at bias voltages of $V_B = -1$ V. The peak detectivity, D^*_λ, can now be calculated from $D^*_\lambda = R\sqrt{A\Delta f}/i_n$ where $A = 1.6 \times 10^{-4} cm^2$ is the device area and $\Delta f = 1$ Hz is the bandwidth. At an operating bias of $V_B = -1$ V and T = 77 K the measured values for the $Al_{0.1}Ga_{0.38}In_{0.52}As$/InP QWIP are R_P = 0.37 A/W, i_n = 80 $pA/Hz^{1/2}$ and thus $D^* = 1 \times 10^9$ $cmHz^{1/2}W^{-1}$. The detectivity of the first sample ($Ga_{0.47}In_{0.53}As$/InP QWIP–A) at T = 77 K and $V_B = -1$ V is $D^* = 4 \times 10^{10}$ $cmHz^{1/2}W^{-1}$.

Using the spectral response data obtained for these samples, it is possible to estimate the conduction band offset for the $Al_xGa_{0.48-x}In_{0.52}As$/InP heterojunction. The cutoff wavelength for samples A, F, and G correspond approximately to the energy separation $\Delta E = E_2 - E_1$ for the three aluminum compositions, y = 0 (A), y = 0.1 (F), and y = 0.15 (G). The energies of the first and second allowed states for these AlGaInAs/InP samples can be calculated for several possible conduction band offsets using the well widths given in Table 2. The E_g of $Al_xGa_{0.48-x}In_{0.52}As$ layers was reported by Fujii et al. [34], and changes linearly from 0.75 eV to 1.47 eV with increasing x. The electron effective mass (m_e) of $Al_xGa_{0.48-x}In_{0.52}As$ layers was reported by Olego et al. [35], and changes linearly from 0.041 to 0.075 with increasing x. In Table 4, the conduction band offset that best fit the cutoff wavelength observed in Fig. 11 are listed.

A plot of the fit conduction band offset as a function of aluminum fraction is shown in Fig. 13. The data from samples A, F, and G are indicated in the figure. The line is the band offset predicted by the Harrison model as applied by Ishikawa et al. [36,37].

From the experimental data for these QWIPs, it would be expected that the transition from type I quantum well to type II staggered quantum well for $Al_xGa_{0.48-x}In_{0.52}As$/InP heterojunctions would occur at x = 0.27. This is below the value (x = 0.33) predicted by the experimental model, which is based on an interpolation from binary data for InAs, GaAs, and

Table 4. Conduction band offset and band offset ratio calculated for samples A, F, and G

Sample	Composition	Well width (Å)	Conduction band offset, ΔE_c	Offset ratio $\Delta E_c/E_G$
A	$Ga_{0.47}In_{0.53}As$	56	229 meV	0.37
F	$Al_{0.1}Ga_{0.38}In_{0.52}As$	60	146 meV	0.29
G	$Al_{0.15}Ga_{0.38}In_{0.52}As$	65	103 meV	0.235

 © 1999 COSiW SEP, Warsaw

AlAs, but larger than other recent experimental results for GSMBE-grown material; x = 0.18 calculated from interband absorption by Kawamura et al. [38], and x = 0.23 calculated from Shottky diode dark currents by Chua et al. [31]. Because intersubband absorption is very sensitive to the conduction band offset, the measurements presented here represent an accurate method for determining this type I–to–type II transition composition.

4.2.4. Dual-colour AlGaInAs/InP QWIPs

A sample was grown for multispectral absorption in both MWIR and LWIR regions by including multiple quantum wells of both $Ga_{0.47}In_{0.53}As/Al_{0.48}In_{0.52}As$ and $Ga_{0.47}In_{0.53}As/InP$. Because the mask utilized in this work allows only one contact to be made to the mesa, the two MQW detectors are placed in series. At low biases, the electric field is applied mostly across the lower-resistance GaInAs/InP MQW. At higher biases, the electric field is applied across both MQWs, but the GaInAs/InP MQW is under such high field that no response is observed. Most carriers in the ground state tunnel out before absorption occurs, resulting in low LWIR photoresponse. A schematic of the processed device is shown in Fig. 14. The spectral response of this dual-band detector is shown in Fig. 15. for several biases. For biases smaller than 10 V, the photoresponse in the 3-5 μm region is too noisy to resolve. For biases greater than ~ 7 V, the photoresponse in the -9 μm region is no longer observed.

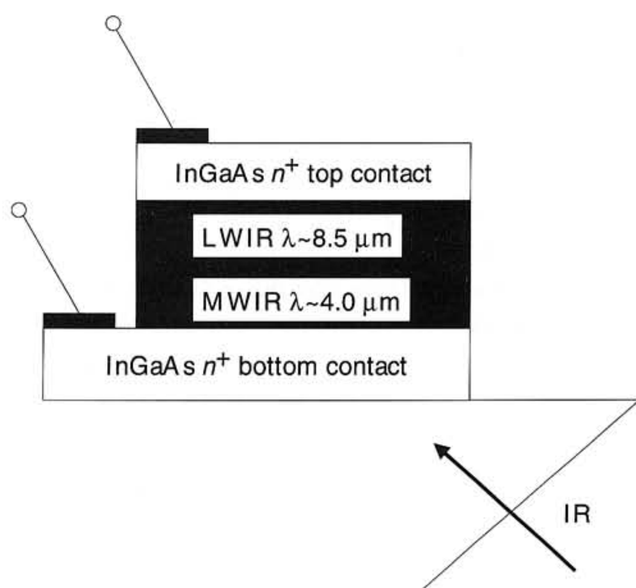

Fig. 14. Schematic diagram of a processed two-colour detector.

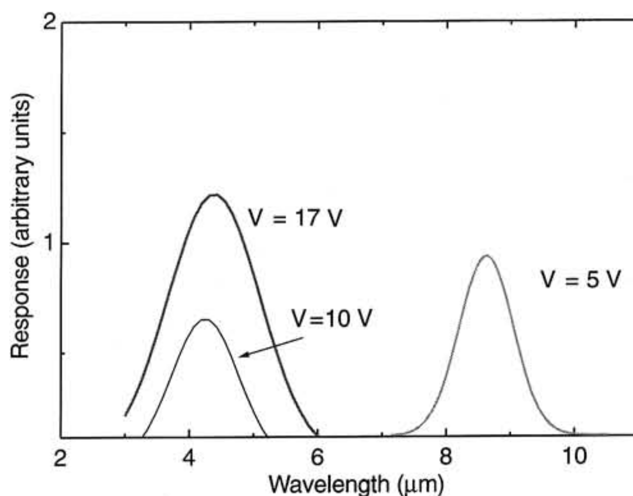

Fig. 15. Voltage dependence of the spectral response for the two-colour detector, measured at T = 77 K.

4.3. Analysis

In order to determine quantitative information about the transport properties of typical QWIP devices, the current and resistance were measured at T = 80 K as functions of applied voltage using an HP 4155A semiconductor parameter analyser with the detectors shielded (i.e. dark). The current-voltage curve for QWIP-A is shown in Fig. 16.

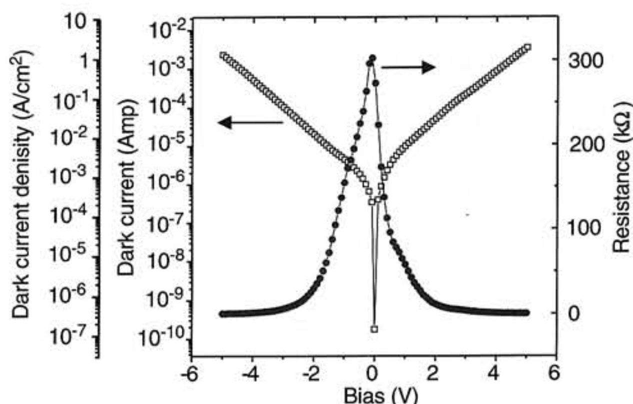

Fig. 16. The dark current and differential resistance vs applied bias for QWIP-A at T = 80 K.

The activation energy, E_A, has been calculated from the slope of ln (I_{DARK}/T) versus 1/T. The result is shown in Fig. 17. An activation energy of 138 meV is obtained for temperatures above 80 K. The expected cutoff wavelength calculated from this energy, λ_c = 8.9 μm, agrees well with the cutoff wavelength of 8.5 μm shown in Fig. 6.

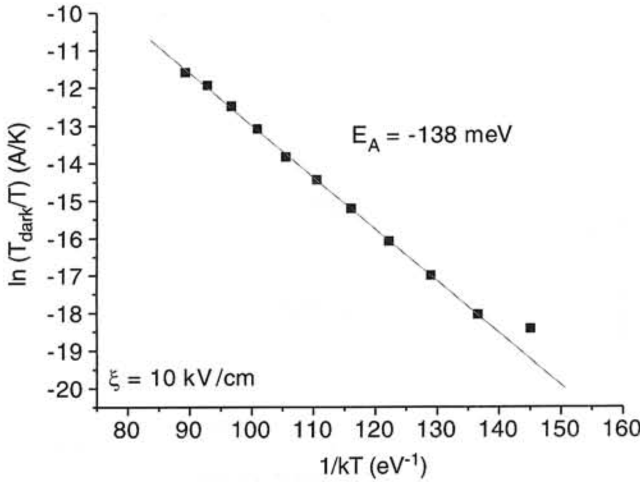

Fig. 17. Activation energy for thermal dark current.

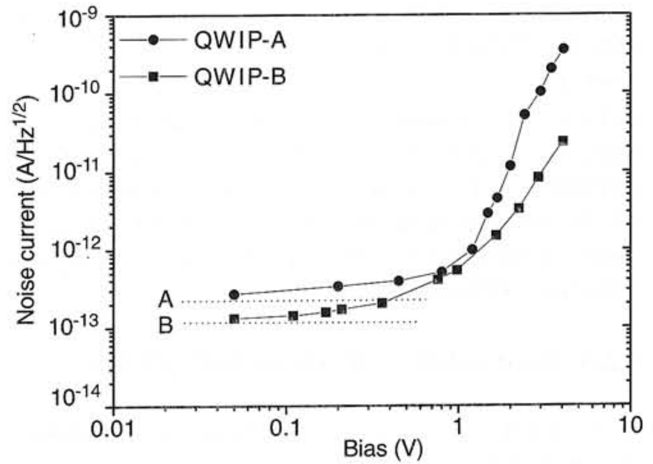

Fig. 19. Noise measurements for QWIPs-A and -B at T = 77 K as a function of bias.

4.3.1. Analysis of the noise spectroscopy data

Current noise

The photocurrent in a QWIP is given by equation (6), where Q is the incoming photon flux, η is the quantum efficiency, and g is the gain of the device. To determine g, dc or noise measurements can be employed. The dc method requires a measurement of the absorbed photon flux, i.e. the product Qη. This measurement is complicated since a fraction of the incoming light is reflected and absolute power levels are difficult to measure accurately. Noise measurements provide an elegant alternative.

Shown in Fig. 18 is the current noise spectrum for QWIP-A at T = 80 K and bias of 0.1 V. The noise measured at frequency f > 100 Hz shows a plateau in the noise spectrum. The decrease for f > 10 kHz is due to the bandwidth limitation of the amplifier. In order to understand the source of noise, the noise current was measured for different bias voltages.

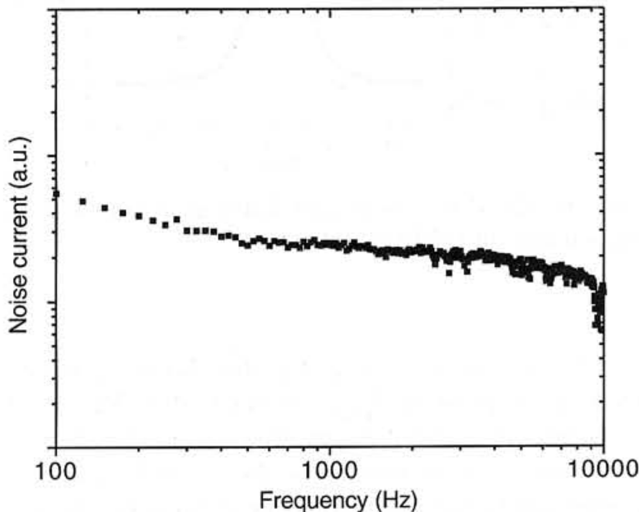

Fig. 18. Noise current spectrum measured for QWIP-A at 0.1 V bias and T = 77 K.

The bias dependence of the magnitude of the noise at 500 Hz is shown in Fig. 19. The QWIP noise current is due to fluctuations in the trapping and de-trapping rates of electrons in the quantum well-bound states, and corresponds to generation-recombination (GR) noise is bulk photoconductors. Two regions in graph are apparent. Near zero bias, the current noise is only weakly dependant on applied bias. In this region, the magnitude of the current noise spectral density conforms to the well-known Nyquist expression as predicted by Rose [39]:

$$S_{Nyquist} = 4k_B T \frac{1}{R_o} \Delta f \tag{7}$$

where k_B is the Boltzmann's constant, and R_o is the small signal resistance given in Fig.16. The noise values calculated for QWIPs A and B using (7) are shown as dotted lines in Fig. 19.

At moderate voltages, the noise current begins to increase with increasing applied bias. The critical bias V_c where the noise current becomes bias dependant is given by [40]:

$$V_c = \frac{k_B T}{eL_D} L_{device} \tag{8}$$

where L_D is the distance travelled by an excited-state electron before it is recaptured by into a quantum well, and L_{device} is the total device length (which

 © 1999 COSiW SEP, Warsaw

equals $(L_W + L_B)N$, where N is the number of periods in the MQW). Although it is difficult to exactly determine V_C from Fig. 19, we infer $V_C \approx 0.2$–0.3 V for both samples. At this bias, the noise current is 2x larger than that predicted by Eq. (7). This results in $L_D \approx 350$–400 Å for both samples. Thus, for bias voltages smaller than V_C, most of excited state electrons are recaptured in the same well they were excited from. This determinism results in an external photocurrent noise dominated by thermal fluctuations. When the critical bias is exceeded, excited electrons transport to the next-nearest neighbour well or farther, and the photocurrent noise due to random fluctuations in the trapping and de-trapping rates of electrons grows rapidly.

Photoconductive gain

The spectral density of the dark current noise associated with the generation-recombination and trapping of carriers in a photoconductor is written as [39]

$$S_{idark} = 4eI_{dark}g_{noise} \tag{9}$$

where g_{noise} is the noise gain. It has been shown that $g_{noise} \cong g_{photo}$ [40]. Accepting the above stated equivalence, the value of g_{photo} for QWIPs A and B have been calculated from noise measurements. Care has been taken in this case to ensure that the noise associated with the trapping and generation is measured, and not excesses 1/f noise or another noise contribution. In Fig. 20 we plot the noise gain for both samples. For both devices the noise gain increases with increasing bias voltage.

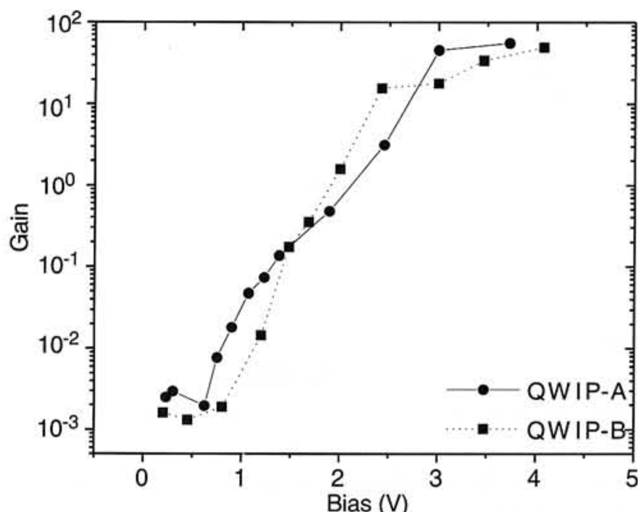

Fig. 20. Photoconductive gain as a function of bias for samples A and B at T = 77 K.

Electron trapping probability

This electron trapping probability can be expressed in terms of the noise gain [41] as

$$p = \frac{1}{1 + Ng} \tag{10}$$

where p is the electron trapping probability of a single well, N is the total number of wells of the device, and g is the gain. The trapping probability versus bias voltage is plotted in Fig. 21.

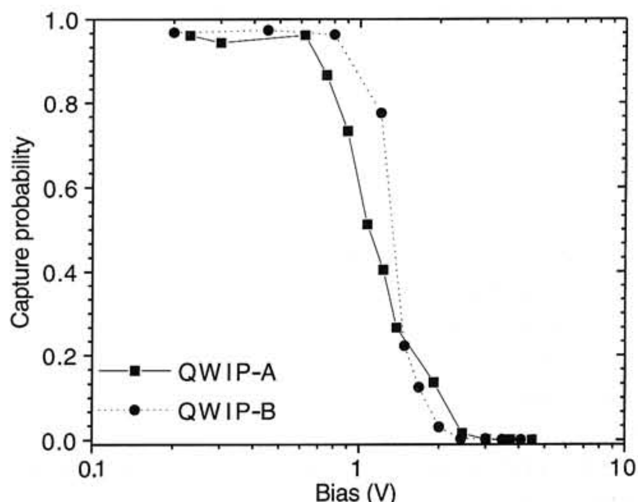

Fig. 21. Electron trapping probability versus applied bias voltage at T = 77 K.

Hence, the following picture emerges. Electrons are thermally generated in the quantum wells, producing locally an excess electron density in the extended conduction states, which subsequently spreads out into the MQW regions. The extended-state electron trajectory L_D, which might be affected by collision and/or tunneling (these noise measurements cannot discriminate between the two modes of transport), is terminated by trapping in a quantum well. At zero or low electric fields, this turns out (on average) to be same quantum-well that the electrons originate from or the next-nearest neighboring well. At higher fields the electron trapping probability becomes smaller due to field-assisted lowering of the MQW barriers, thereby improving the coupling to the external circuit and increasing the gain and current noise level.

Theoretical interpretation

We define the electron lifetime in the conduction band to be τ_o, and in the ground state of the QW to be τ_w. We also define the total number of electrons in the

conduction band to be P_o, and in the well is P_W. In equilibrium, the average number of electrons generated from the QW ground state should equal the average number of electrons recombining from the valence-band extended states. Thus

$$G = R \text{ or } \frac{P_W}{\tau_W} = \frac{P_o}{\tau_o} \tag{11}$$

The particle number spectral density $\langle \Delta P \rangle^2 = S_p(f)\Delta f$ where $S_P(f)$ is according to van der Ziel [42]

$$S_p(f) = 4G\frac{\tau^2}{1+\omega^2\tau^2} \tag{12}$$

where $\tau \approx \tau_o + \tau_W$, and G is the electron generation rate (s^{-1}) from the quantum well ground state to the conduction band extended state.

At low temperatures, the total number of holes in the conduction band is much smaller than the number of electrons in the QW ground state because the barriers are undoped. Therefore $\tau_o << \tau_W$, resulting in $\tau \approx \tau_o$. This implies that the particle number spectral density at low frequencies is

$$S_p(0) = 4Gt_o^2 \tag{13}$$

In these n–type QWIPs with undoped barriers, the number of mobile electrons in the conduction band is equal to the number of electrons excited from the quantum well ground state (assuming there are no trap states emitting carriers). Therefore, dark current is defined as

$$I_d = Aenv = ev\frac{P_o}{L} \tag{14}$$

Here v is the average electron velocity, n is the carrier concentration in the conduction band, L is the total device length. Using the photoconductive gain, defined as $g = v\tau_o/L$, Eq. (6), the dark current can also be written as

$$I_d = ev\frac{P_o}{L} = eg\frac{P_o}{t_o} = egG \tag{15}$$

Current fluctuations are related to number fluctuations by equation (14), i.e., $\Delta I = (ev/L)\Delta P_o$. Thus, the current noise spectral density S_i is defined as

$$S_i = \langle Di \rangle^2 = \left(\frac{ev}{L}\right)^2 S_p. \tag{16}$$

In the absence of an applied electric field, the diffusion length L_D is the distance a carrier diffuses before recombining into quantum well ground states. Therefore the current noise in the diffusion dominant regime can be expressed as

$$S_i = 4e^2G\left(\frac{\tau_o v}{L}\right)^2 = 4e^2G\left(\frac{L_D}{L}\right)^2 \tag{17}$$

When a sufficient bias is applied, transport is drift dominated and equation (17) no longer applies.

By combining equations (11), (14), and (15), the current noise spectral density can be expressed as

$$S_i = 4\left(\frac{ev}{L}\right)^2\frac{P_o^2}{G} = \frac{4I_d^2}{G} \tag{18}$$

As a result, the current noise in the drift dominant regime is proportional to the dark current squared. By substituting equation (15) into equation (18), it is obvious that the current noise power spectral density is proportional to the electron generation rate G

$$S_i = 4g^2e^2G \tag{19}$$

Thus the noise current spectral density, i_n, defined by $\langle i_n \rangle^2 = S_i(f)\Delta f$, is given by

$$\frac{i_n}{\Delta f^{1/2}} = 2ge\sqrt{G} \tag{20}$$

The specific detectivity of a detector is defined as $D^* = R_i A^{1/2}\Delta f/i_n$. Using equations (6) and (20), it can be re-written as

$$D^* = \frac{\eta\lambda A^{1/2}}{2\sqrt{G}} \tag{21}$$

Thus a smaller generation rate is directly linked to the higher detector detectivity.

It is possible to model the generation rate if we assume the generation rate of electrons from the ground state of the quantum well is the same as the emission of electrons from a trap state to the conduction band [43], so that

$$1/\tau_{escape} = v_{th}\sigma_e N_c e^{-\Delta E/kT} \tag{22}$$

 © 1999 COSiW SEP, Warsaw

where v_{th} is the thermal velocity of the electron, ΔE is the energy from the QW ground state to the barrier conduction band, σ_e is the capture cross section of the trap, and N_c is the effective density of states in the conduction band. The generation rate density for the whole quantum well is defined as

$$g = \frac{N_p}{\tau} = N_D v_{th} \sigma_e N_c e^{-\Delta E/kT} \qquad (23)$$

The generation rate density can thus be written $g = Ce^{-\Delta E/kT}$, where C is the electron generation rate constant (in $cm^{-3}s^{-1}$). The total electron generation rate is

$$G = NAL_W g \qquad (24)$$

where N is the number of periods of quantum wells, A is the area, and L_W is the quantum well width.

Furthermore, it is possible to model the expected capture cross-section by assuming a model of carrier recombination due to coulombic attraction to donor atoms. Thermally generated electrons move via drift or diffusion in the barrier region to a neighboring quantum well. These wells are doped with silicon donors to a concentration of $\sim 1 \times 10^{18}$ cm^{-3}, which results in an inter-donor spacing of about 50 Å. Since the well width is only 50 Å, these donors basically form a monolayer thin plane of charge centers. The electrons approaching this monolayer with a thermal velocity determined by barrier parameters will interact with these silicon centers triggering a recombination process which results in the electrons reaching the E_1 bound state. Assuming ineffective screening of the silicon nuclei due to the two-dimensionality of the surrounding electron gas, we approximate the silicon perturbation potential by $Zq/4\pi\varepsilon_o\varepsilon_r r$ where Z is the atomic number of silicon, equal to 14 [43]. The holes impinging on the silicon centers gain kinetic energy by crossing the well/barrier interface. Hence to determine the effective scattering cross section σ_e of the silicon centers embedded in the quantum wells, we can equate

$$\frac{Ze^2}{4\pi\varepsilon_o\varepsilon_r r} = \Delta E \qquad (25)$$

The scattering cross section $\sigma_e = \pi r^2$ can then be calculated. This equation implies that electrons with energy higher than the right-hand side of equation (25) do not sense the perturbation potential and are not scattered. For a temperature of T = 77 K, and using ε_r = 13.7 and ΔE = 138 meV (see Fig. 17) for $Ga_{0.47}In_{0.53}As$, this model predicts a scattering cross section of $\sigma_e = 3.6 \times 10^{-12}$ cm^2.

Experimental noise analysis

The noise current spectral density versus dark current is plotted in Fig. 22 for QWIP–A.

The solid line illustrates the I^2 dependency predicted by equation (18). For high dark currents, the slight deviation of the measured curve from the I^2 dependence is attributed to an increase in the thermal generation rate. This effect is highlighted in Fig. 23 where the natural logarithm of the thermal generation rate G, calculated from equation (18), is plotted versus applied bias voltage. The calculated generation rate is 4×10^{22} $cm^{-3}s^{-1}$. The solid line is the best linear fit to ln(G) versus bias and has a slope of 0.47 V^{-1}.

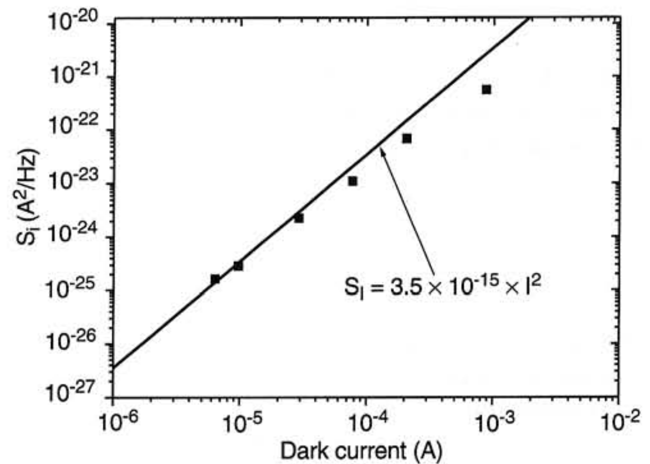

Fig. 22. Current noise spectral density versus dark current at T = 80 K for sample A.

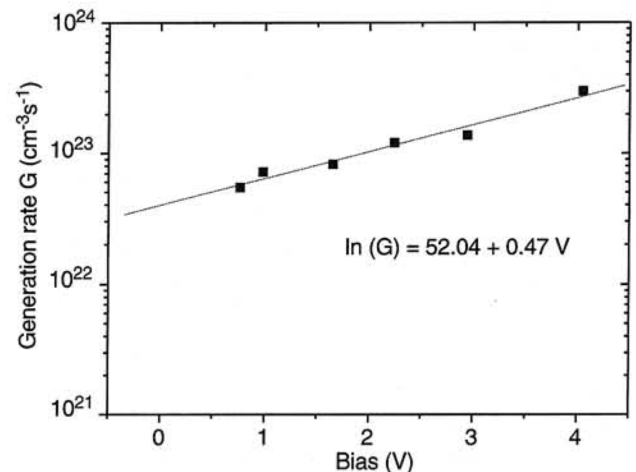

Fig. 23. Calculated thermal generation rate versus applied bias at T = 77 K for sample A.

From a simple charge balance model for heavily doped quantum wells it follows that

$$G = e_n n_w = c_n n_w N_c e^{-E_A/kT} = c_n n_d N_c e^{-E_A/kT} \quad (26)$$

where e_n is the bound electron emission coefficient, c_n is the electron capture coefficient, n_w is the electron density in the quantum well ground state, N_c is the effective density of states of the continuum above the well, and E_A is the bound electron activation energy, equal to 138 meV for these samples in equilibrium (see Fig. 17). Upon applying bias, band bending will occur, leading to lower activation energy because electrons can escape via the lowered side (in energy) of the quantum well. With a voltage drop V_W across a quantum well, a first order for an upper estimate of the effect is

$$E_A = E_A^0 - eV_W \quad (27)$$

where E_A^0 is the zero bias activation energy. Assuming a constant electric field throughout the device, including the quantum well regions,

$$V_W = \frac{V_W}{L_p N} \quad (28)$$

where V is the applied bias voltage, and L_p is the length of a period. Solving equations (26) through (28) results in

$$\ln(G) = \ln(c_n n_d N_c) - \frac{E_A^0}{kT} + \frac{ewV}{kTL_p N} \quad (29)$$

predicting a linear dependence of ln(G) with V with a slope of 0.73, which is slightly larger than the measured value. This discrepancy may be due to the spatial dependence of bound electron generation. Theoretically, the highest electron concentration and thus generation rate is expected at or near the center of the quantum well where electrons will only experience a fraction of the band lowering. In addition, the electric field in the quantum well region may be lower than in the barrier. This will also lead to a smaller slope of ln(G) versus V.

The generation rate constant C for sample A was found by fitting equation (18) and (19) to the noise power spectral density shown in Fig. 22. The best is for $C = 2.5\times10^{31}$ $cm^{-3}s^{-1}$. Figure 24 shows the measured noise values (squares) versus applied bias voltage as well as the fit made using equation (17) and (18). Note that equation (18) explains the magnitude for the noise very well for the drift dominated regime. The same value of C was used with equation (17) to fit the noise data in the diffusion dominant regime. The diffusion length L_D which gave the best fit for this value of C was L_D = 500 Å, which is very similar to the diffusion length of 400 Å determined using equation (8).

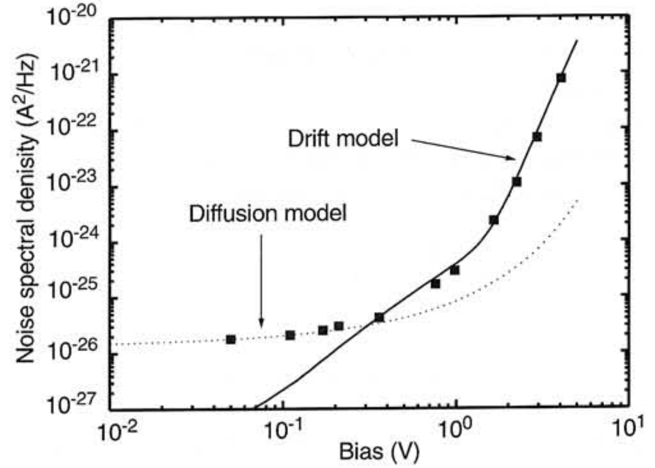

Fig. 24. Experimental and theoretical current noise spectral density versus bias voltage at T = 77 K for sample A.

A value of $\sigma_e = 9.4\times10^{-12}$ cm^2 is calculated for the capture cross section using equation (23) and $C = 2.5\times10^{31}$ $cm^{-3}s^{-1}$. This calculation used $N_D = 8\times10^{17}$ cm^{-3} and bulk values of N_c and ν_{th} for $In_{0.53}Ga_{0.47}As$. This agrees well (2.5 × higher) with the values of 3.6×10^{-12} cm^2 obtained from the simple model of equation (25). The slightly higher measured scattering cross section may indicate the presence of some interface roughness-related or alloy scattering in addition to the modeled coulombic scattering.

Comparison to GaAs/AlGaAs

It is interesting to compare the thermal generation rate, gain, and capture probability measured for these samples with values previously published for AlGaAs/GaAs samples. For detectors with a similar peak absorption wavelength near 8 μm, Wang et al. [40,41] have measured a generation/recombination rate of 1.5×10^{23} $cm^{-3}s^{-1}$ in GaAs/ AlGaAs samples. Using equation (21), the 4 × lower recombination rate for these InGaAs/InP samples should result in the 2 × higher peak detectivity for detectors with similar areas at the same wavelength. This agrees fairly well with the published maximum peak detectivities for GaAs/AlGaAs detectors by Levine et al. [3] (1×10^{10} $cmHz^{1/2}W^{-1}$) and Claiborne et al. [44] (3×10^{10} $cmHz^{1/2}W^{-1}$) as compared to the peak detectivities for

 © 1999 COSiW SEP, Warsaw

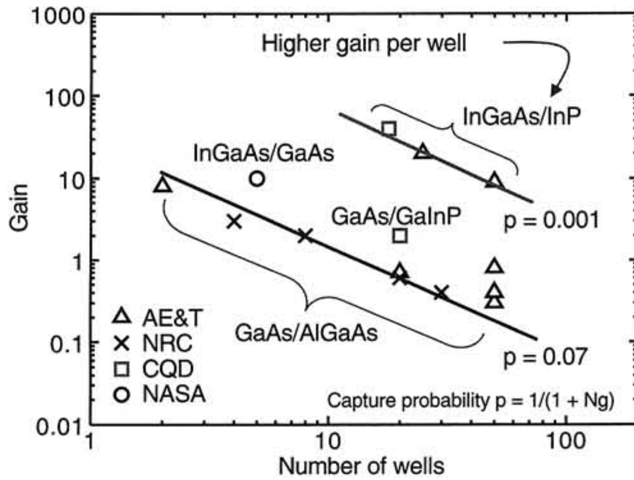

Fig. 25. Photoconductive gain versus number of quantum wells for various QWIP systems.

InGaAs/InP detectors in this work (6×10^{10} cmHz$^{1/2}$W^{-1}) and Gunapala et al. [11] (9×10^{10} cmHz$^{1/2}$W^{-1}). It is hypothesized here that the recombination rates are larger in GaAs/AlGaAs heterostructures due to larger scattering cross sections from larger interface roughness in a ternary material or the presence of aluminum related DX–center traps.

A comparison of the photoconductive gain measured for different QWIP materials is shown in Fig. 25. As discussed above, the higher gain in InP-barrier QWIPs is probably due to the longer carrier lifetime (because of a lower recombination rate) and higher drift velocity in the InP barriers, and perhaps a decrease in the number of scattering centers due to the high quality of the binary barrier material.

The increased gain results in a higher detector responsivity. The responsivity for sample E is larger compared with GaAs/AlGaAs devices by Gunapala et al. [45]. This is shown in Fig. 26.

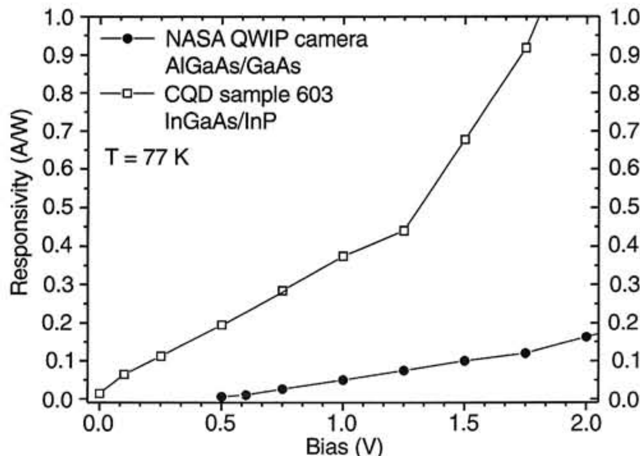

Fig. 26. InGaAs/InP QWIP (sample E) responsivity compared to GaAs/AlGaAs QWIP (after Ref. 45).

5. Conclusions

In conclusion, we have demonstrated the firs QWIP detectors using the quaternary $Al_xGa_yIn_{1-x-y}As$ InP materials system. We have observed excellent responsivity in the $Al_xGa_yIn_{1-x-y}As$/InP devices compared to GaAs/AlGaAs QWIPs. By increasing the bandgap from ternary $Ga_{0.47}In_{0.53}As$ to quaternary $Al_xGa_{0.48-x}In_{0.52}As$ we have shifted the responsivity out to longer wavelengths resulting in cutoff wavelengths of 13.3 and 19.4 μm, respectively for AlAs mole fractions of 0.1 and 0.15. We have also demonstrated lattice-matched mid-wavelength infrared detectors using $Ga_{0.47}In_{0.53}As/Al_{0.48}In_{0.52}As$ quantum wells. By combining both types of devices, we have produced the first lattice-matched dual band mid-wavelength and long-wavelength QWIP detectors on InP substrate. Using the measured noise data for $Ga_{0.47}In_{0.53}As$/InP detectors, we have calculated the thermal generation rate, bias-dependent gain, electron trapping probability, and electron diffusion length. The calculated thermal generation rate (~ 7×10^{22} cm^{-3}s^{-1}) is similar to $Al_xGa_{1-x}As$/GaAs QWIPs with similar peak wavelengths, but the gain is 50 × larger, indicating improved transport and carrier lifetime are obtained in the binary InP barriers.

Acknowledgements

The authors would like to acknowledge the support of Dr. Gerald Witt and Dr. Michael Prairie of the Air Force Office of Scientific Research (AFOSR). The authors would like to thank Lew Loem of the Ballistic Missile Defense Organization (BMDO) and L.N. Durvasula of Defense Advanced Research Project Agency (DARPA) for their continued support and encouragement. This work was supported by the Air Force under the contracts No. F49620-97-1-0288 and No. F49620-97-0422.

References

1. L. West and S. Eglash, "First observation of an extremely large dipole infrared transition within the conduction band of a GaAs quantum well," *Appl. Phys. Lett.* **46**, 1156 (1985).
2. W.A. Beck and T.S. Faska, "Current status of quantum well focal plane arrays," *Proc. SPIE* **2744**, 192 (1996).
3. B. Levine, "Quantum well infrared photodetectors," *J. Appl. Phys.* **74**, R1 (1994).
4. D. Ritter, R.A. Hamm, M.B. Panish, J.M.

Vandenberg, D. Gershoni, S.D. Gunapala, and B.F. Levine, "Metalorganic molecular beam epitaxial growth of InP/InGaAs multiquantum wells for infrared detection," *Appl. Phys. Lett.* **59**, 552 (1991).
5. S.D. Gunapala, B.F. Levine, D. Ritter, R.A. Hamm, and M.B. Panish, "Lattice-matched InGaAsP/InP long-wavelength quantum well infrared photodetectors," *Appl. Phys. Lett.* **60**, 636 (1992).
6. L.L. Change, L. Esaki, and G.A. Sai-Halaz, *IBM Technical Disclosure Bulletin* **20**, 2019 (1987).
7. L. Esaki and H. Sakaki, *IBM Technical Disclosure Bulletin* **20**, 2456 (1977).
8. B.F. Levine, K.K. Choi, C.G. Bethea, J. Walker, and R.J. Malik, *Appl. Phys. Lett.* **50**, 1092 (1987).
9. S.D. Gunapala and K.M.S.V. Bandara, "Recent developments in quantum well infrared photodetectors" in *Thin Films*, Vol. 21, p. 113, edited by M.H. Francombe, Academic Press, San Diego, 1995.
10. S.D. Gunapala, B.F. Levine, D.L. Silco, and A.Y. Cho, "Mid-infrared detectors in the 3–5 μm band using bound-to-continuum state absorption in InGaAs/InAlAs multiquantum well structures," *Appl. Phys. Lett.* **56**, 770 (1990).
11. S.D. Gunapala, B.F. Levine, D. Ritter, R. Hamm, and M.B. Panish, "InGaAs/InP long wavelength quantum well infrared photodetectors," *Appl. Phys. Lett.* **58**, 2024 (1991).
12. C. Jelen, S. Slivken, T. David and M. Razeghi, "Multispectral InP-based quantum well infrared photodetectors" *International Semiconductor Devices Research Symposium Proc.*, Charlottesville, VA: UVA Press, (1997).
13. C. Jelen, S. Slivken, T. David and M. Razeghi, "High responsivity InGaAs/InP QWIPs grown using gas-source molecular beam epitaxy, *Proc. SPIE* **3287,** (1998).
14. C. Jelen, S. Slivken, T. David, and M. Razeghi, "Noise performance of InGaAs/InP quantum well infrared photodetectors," accepted for publication in *IEEE J. Quant. Electron.* (1998).
15. C. Jelen, S. Slivken, J. Hoff, G.J. Brown, and M. Razeghi, "Aluminum free GaInP/GaAs quantum well infrared photodetectors for long wavelength detection," *Appl. Phys. Lett.* **70**, 360–362 (1997).
16. C. Jelen, S. Slivken, G. Brown, M. Razghi, "GaAs/GaInP Quantum well intersubband photodetectors for focal plane array infrared imaging," *MRS Proc.* **450**, 195-199 (1997).
17. C. Jelen, S. Slivken, G. Brown, M. Razghi, "Very long wavelength GaAs/GaInP quantum well infrared photodetectors," *Proc. SPIE* **2999**, 144 (1997).
18. S.D. Gunapala, B.F. Levine, R.A. Logan, T. Tanbum-Ek, and D.A. Humphrey, "GaAs/GaInP multiquantum well long-wavelength infrared detector using bound-to-continuum absorption," *Appl. Phys. Lett.* **57**, 1802 (1990).
19. J. Hoff, C. Jelen, S. Slivken, O. Duchemin, E. Bigan, M.Razghi, G. Brown, and S. Hegde, "Intersubband hole absorption in GaAs-GaInP quantum wells grown by gas-source molecular beam epitaxy," *Appl. Phys. Lett.* **65**, 1130–1132 (1994).
20. R.P.G. Karunasiri, J.S. Park, and K.L. Wang, "Progress of SiGe/Si quantum well for infrared detection," in *Thin Films,* Vol. **21**, pp. 113–237, edited by M.H. Francombe and J.L. Vossen, Academic Press, San Diego, 1995.
21. K.K. Choi, *The Physics of Quantum Well Infrared Photodetectors*, Vol. 7, Series in Modern Condensed Matter Physics, edited by I. Dzyaloshinshi, S. Lundqvist, and Yu Lu, World Scientific, Singapore, 1997.
22. B.F. Levine, R.J. Malik, J. Walker, K.K. Choi, C.G. Bethea, D.A. Kleinman, and J.M. Vandenberg, "Strong 8.2 m infrared intersubband absorption in doped GaAs/AlAs quantum well waveguides," *Appl. Phys. Lett.* **50**, 273 (1987).
23. C.J. Chen, K.K. Choi, M.Z. Tidrow, and D.C. Tsui, "Corrugated quantum well infrared photodetectors for normal incident light coupling," *Appl. Phys. Lett.* **68**, 1446 (1996).
24. G. Sarusi, B.F. Levine, S.J. Pearton, K.M.S.V. Bandara, and R.E. Leibenguth, "Optimization of two-dimensional gratings for very long wavelength quantum well infrared photodetectors", *J. Appl. Phys.* **76**, 4989 (1994).
25. G. Sarusi, B.F. Levine, S.J. Pearton, K.M.S.V. Bandara, and R.E. Leibenguth, "Improved performance of quantum well infrared photodetectors using random scattering optical gratings," *Appl. Phys. Lett.* **64**, 960 (1994).
26. J. Andersson, L. Lundqvist and Z.F. Paska, "Quantum efficiency enhancement of AlGaAs/GaAs quantum well detectors using a waveguide with a grating coupler," *Appl. Phys. Lett.* **58**, 2264 (1991).
27. J. Andersson, L. Lundqvist and Z.F. Paska, "Grating coupled quantum well infrared photo-

 © 1999 COSiW SEP, Warsaw

detectors: theory and practice," *J. Appl. Phys.* **71**, 3600 (1991).

28. R.J. Malik, J.R. Hayes, F. Capasso, K. Alavi, and A.Y. Cho, "High-gain AlInAs/GaInAs vertical n-p-n heterojunction bipolar transistors grown by molecular beam epitaxy," *IEEE Electron. Dev. Lett.* **EDL-4**, 383 (1983).
29. W. Lee and C.G. Fonstad, "O^+ implantation and annealing in n–type InAlAs," Appl. *Phys. Lett.* **50**, 1278 (1987).
30. J. M. Kuo, T.Y. Chang, and B. Lalevic, "GaInAs/AlInAs pseudomorphic modulation-doped field effect transistors," *IEEE Electron. Dev. Lett.* **EDL-8**, 380 (1987).
31. S.J. Chua and A. Ramam, *Proceedings of the 1996 IEEE International Conference on Semiconductor Electronics,* Piscataway, NJ: SPIE Press, 469–471, 1994.
32. H. Kroemer and G. Griffiths, "Staggered lineup heterojunctions as sources of tunable below-gap radiation: operating principles and semiconductor selection," *IEEE Electron Device Lett.* **EDL-4**, 20 (1983).
33. C. Chen, K. Choi, M. Tidrow, and D. Tsui, *Appl. Phys. Lett.* **68**, 1446 (1996).
34. T. Fujii, Y. Nakata, Y. Sugiyama, and S. Hiyamizu, "MBE growth of InGaAlAs lattice--matched to InP by pulsed molecular beam method," *Jpn. J. Appl. Phys.* **25**, No. 3, L254–L256 (1986).
35. D. Olego, T.Y. Chang, E. Silberg, E.A. Caridi and A. Pinkzuk, "Compositional dependance of band-gap energy and conduction band effective mass of $In_{1-x-y}Ga_xAl_yAs$ lattice-matched to InP," *Appl. Phys. Lett.* **41**, 476–478 (1982).
36. T. Ishikawa and J.E. Bowers, "Band lineup and in-plane effective mass of InGaAsP or InGaAlAs on InP strained-layer quantum well," *IEEE J. Quant. Electron.* **30**, 562–570, (1994).
37. W.A. Harrison, "Elementary theory of heterojunctions," *J. Vac. Sci. Technol.* **14**, 1016–1021, (1977).
38. Y. Kawamura, H. Kobayahsi, and H. Iwamura, "Type I/Type II transition in InGaAlAs/InP multiple quantum well structures grown by gas--source molecular beam epitaxy," *Jpn. J. Appl. Phys.* **33**, L79–L82 (1994).
39. A. Rose, *Concepts in Photoconductivity and Allied Problems*, John Wiley & Sons, New York, 1963.
40. D. Wang, Y. Wang, G. Bosman, and S. Li, "Noise in physical systems and 1/f fluctuations", *AIP Conf. Proc.*, 415 (1993).
41. D. Wang, G. Bosman, Y. Wang, and S. Li, "Noise performance of bound-to-miniband transition III–V quantum well infrared photodetectors," *J. Appl. Phys.* **77**, 1107 (1995).
42. Aldert van der Ziel, *Noise in Solid State Devices and Circuits*, John Wiley & Sons, New York, 1986.
43. R. H. Bube, *Photoelectrical Properties of Semiconductors*, Cambridge University Press, Cambridge, 1992.
44. L.T. Claiborne and M.A. Dodd, "Improved performance III–V quantum well infrared photodetectors: review of current and potential focal plane technology," *Proc. SPIE* **2999,** 32 (1997).
45. S.D. Gunapala, J.K. Liu, J.S. Park, M. Sundaram, C.A. Shott, T. Hoelter, T. Lin, S.T. Massie, P.D. Maker, R.E. Muller, and G. Sarusi, "9–μm cutoff 256 × 256 $GaAs/Al_xGa_{1-x}As$ quantum well infrared photodetector hand-held camera," *IEEE Trans. Electr. Dev.* **44**, 51–57 (1997).